

# Numerical study on the axial segregation dynamics of a binary-size granular mixture in a three-dimensional rotating drum

Shiliang Yang, Yuhao Sun, Liangqi Zhang, and Jia Wei Chew

Citation: *Physics of Fluids* **29**, 103302 (2017); doi: 10.1063/1.5004663

View online: <http://dx.doi.org/10.1063/1.5004663>

View Table of Contents: <http://aip.scitation.org/toc/phf/29/10>

Published by the American Institute of Physics

---

## Articles you may be interested in

[Hydrodynamic interactions between a self-rotation rotator and passive particles](#)

*Physics of Fluids* **29**, 103301 (2017); 10.1063/1.4997221

[Impact zone dynamics of dilute mono- and polydisperse jets and their implications for the initial conditions of pyroclastic density currents](#)

*Physics of Fluids* **29**, 093304 (2017); 10.1063/1.5004197

[Unified gas-kinetic scheme with multigrid convergence for rarefied flow study](#)

*Physics of Fluids* **29**, 096102 (2017); 10.1063/1.4994020

[An experimental study on the drop/interface partial coalescence with surfactants](#)

*Physics of Fluids* **29**, 102101 (2017); 10.1063/1.4985997

[Surface-conduction enhanced dielectrophoretic-like particle migration in electric-field driven fluid flow through a straight rectangular microchannel](#)

*Physics of Fluids* **29**, 102001 (2017); 10.1063/1.4996191

[Effect of a planar interface on time-averaged locomotion of a spherical squirmer in a viscoelastic fluid](#)

*Physics of Fluids* **29**, 093104 (2017); 10.1063/1.5002574

---

**COMPLETELY  
REDESIGNED!**



**PHYSICS  
TODAY**

*Physics Today* Buyer's Guide  
Search with a purpose.

# Numerical study on the axial segregation dynamics of a binary-size granular mixture in a three-dimensional rotating drum

Shiliang Yang,<sup>1</sup> Yuhao Sun,<sup>2</sup> Liangqi Zhang,<sup>1</sup> and Jia Wei Chew<sup>1,3,a)</sup>

<sup>1</sup>School of Chemical and Biomedical Engineering, Nanyang Technological University, Singapore 637459, Singapore

<sup>2</sup>Department of Engineering, University of Cambridge, Cambridge CB3 0FA, United Kingdom

<sup>3</sup>Singapore Membrane Technology Center, Nanyang Environment and Water Research Institute, Nanyang Technological University, Singapore 637141, Singapore

(Received 10 May 2017; accepted 12 September 2017; published online 5 October 2017)

Granular materials are ubiquitous in our daily life and inherent in multitudinous industrial processes. Differences in the granular properties such as size and density inevitably induce segregation. By means of the discrete element method, a binary-size mixture in a three-dimensional rotating drum is numerically simulated to explore the segregation dynamics of the granular material along the axial direction. Snapshots of the distribution of the two particle types in the rotating drum are presented with respect to time to illustrate the spatial evolution of the size-induced segregation structure. The space-time plots of various axial characteristics indicate that (i) radial segregation does not affect the axial distribution of total mass and mass fraction, but axial segregation leads to the formation of axial bands; (ii) greater non-dimensionalized collision forces for both the large and small particles develop where the large particles dominate; and (iii) axial segregation gives rise to the variation of the gyration radii of both particle types along the drum length. In addition, axial flow of both particle types in both directions indicates the dynamic axial exchanges, and the effect of the end walls on the axial flow direction is limited to less than 25% of the drum length from the end walls. Published by AIP Publishing. <https://doi.org/10.1063/1.5004663>

## I. INTRODUCTION

The rotating drum has gained significant attention due to its importance in understanding the fundamental mechanism of granular flow from both the perspectives of basic science and also of valuable contribution to process operation in the industrial applications.<sup>1</sup> Especially for the latter, an in-depth fundamental knowledge of the dominant phenomena occurring within the rotating drum is required to have the predictive capability on the flow behavior in order to optimise the process design, control, and system efficiency in practical operations. When particles of different size or density are present in the rotating drum, it is inevitable that the difference of the particle properties leads to the radial segregation and axial segregation of the different particle types. The segregation is commonly acknowledged to result in a configuration comprising a radial core of smaller particles surrounded by larger particles in the transverse plane, and alternate bands of large and small particles along the axial direction.<sup>2</sup> Regarding the radial segregation of granular material differing in size in the rotating drum, it is widely accepted that the most dominant mechanism is percolation, which is the phenomena whereby the smaller particles fall through the interstitial voids between larger particles.<sup>1,3</sup> To date, multiple aspects tied to radial segregation have been studied, including the segregation flux of cascading layer,<sup>3</sup> material transport model,<sup>4</sup> the effect of

non-circular geometry,<sup>5,6</sup> the competition of mixing and segregation,<sup>7</sup> the turnover time ratio,<sup>8</sup> the effect of the combination of size and density,<sup>9</sup> radial segregation pattern,<sup>10–12</sup> segregation kinematics,<sup>13</sup> segregation of the ternary-size mixture,<sup>14</sup> and the effect of periodic modulation.<sup>15</sup> Notably, the phenomenon of axial segregation was first reported by Oyama<sup>16</sup> on his experimental work with bidisperse mixtures of limestone particles but has not attracted too much attention until recent decades.<sup>1,17</sup> The focus of the current work is on the size-induced axial segregation of granular material in the rotating drum. Accordingly, the experimental and numerical work pertaining to the axial granular segregation in the rotating drum are reviewed.

The experimental work of Gupta *et al.*<sup>2</sup> showed that a necessary though not sufficient condition for the axial segregation is a difference in the free surface angles of the two constituents in the rotating drum at a particular rotating speed. Also, the bi-directional travelling wave was observed in the experiments conducted by Choo *et al.*<sup>18</sup> Using the positron emission particle tracking (PEPT) technique, Ding *et al.*<sup>8</sup> experimentally tracked the trajectories of particles of different sizes to study segregation dynamics and also to explore the effects of operating parameters on the formation of axial bands in the rotating drum. The results demonstrated that the axial particle mobility increases with the drum rotating speed and the dimensionless bandwidth decreases as the fill level increases. The experimental work of Khan *et al.*<sup>19</sup> concluded that the oscillatory behavior of the segregation process in the rotating drum emerges from the three-dimensional

<sup>a)</sup>Author to whom correspondence should be addressed: JC Chew@ntu.edu.sg.  
Tel.: +65 6316 8916

evolution of the local concentration alone. To investigate the effect of operating parameters and particle property on the axially segregated bandwidth, Kuo *et al.*<sup>20</sup> conducted experiments of binary-size mixtures in a rotating drum and demonstrated that there exists a size ratio whereby the dimensionless bandwidth has a minimum value, which can be attributed to the diffusion and inertial mechanisms of the motion of each particle. Juarez *et al.*<sup>21</sup> experimentally studied the behavior of the axial bands in the rotating drum and found that the bandwidth scales with the drum diameter. To explore the effect of polydispersity on granular flow and segregation, Alizadeh *et al.*<sup>22</sup> conducted experiments with a polydisperse particle size distribution and revealed similar velocity profiles and residence times for monodisperse and polydisperse systems. Using magnetic resonance imaging, Fischer *et al.*<sup>23</sup> experimentally explored the axial dispersion behavior of binary-size mixtures in the rotating drum and found that the small size particles in a radially segregated structure undergo normal axial diffusion. Recent experimental work of Tilo *et al.*<sup>24</sup> focused on the long-term coarsening behavior in a rotating drum and demonstrated that the unidirectional flow between the axial bands is driven by small differences in the sizes of the small particles at the band edges. Furthermore, Windows-Yule *et al.*<sup>25</sup> experimentally studied the axial segregation in a rotating drum and found that it is possible to customize the segregation behavior to induce an arbitrary number of pre-determined segregation patterns in a system.

In the past two decades, the advancement of the computational hardware and numerical algorithm has led to the increasing popularity of the numerical modeling of the dense granular flow.<sup>26</sup> One simulation technique, the discrete element method (DEM) initially proposed by Cundall and Strack,<sup>27</sup> has frequently been adopted to study the granular flow in the rotating drum due to its ability to track the trajectory of all particles at each time instant and make measurements that are difficult to obtain experimentally. The DEM thus serves as a valuable complementary tool to the experimental method in exploring the fundamental mechanism underlying the various phenomena in the rotating drum. Over the last decade, this numerical technique has been successfully used to reproduce the well-known particle flow behavior experimentally observed in the rotating drum and notably also applied to shed light on the axial segregation phenomenon.

Rapaport<sup>28</sup> used DEM to investigate the axial granular segregation in the rotating drum containing a mixture of two different sizes of particles, and the results displayed a variety of phenomena that mostly correspond to what has been observed experimentally. Furthermore, he numerically studied the segregation behavior of three different particle species in a horizontal rotating drum and found that the particles of the intermediate size tend to be located between the alternating bands of large and small particles.<sup>29</sup> Combined with the experimental approach, the numerical simulation conducted by Taberlet *et al.*<sup>30</sup> regarding axial segregation in the rotating drum indicated that the coarsening of axial bands involves flows of small particles through the radial core. To explore the mechanism for band formation of a granular mixture, Chen *et al.*<sup>17</sup> numerically modeled the solid flow in the rotating drum using DEM and found that the end walls initiate

the axial band formation via an axial flow stemming from the friction at the end walls. Recently, by means of parallel computation, Alizadeh *et al.*<sup>31</sup> numerically tracked the solid flow in the rotating drum with a polydisperse particle size distribution to assess the accuracy of the DEM for the simulation of solid mixing, and proposed dimensionless motion equations and corresponding dimensionless numbers to investigate the effect of simulation parameters on the particle dynamics.

Despite the wealth of knowledge gained to date through the experimental and numerical reports on the axial segregation phenomenon in the rotating drum, the understanding of the mechanisms underlying this complex behavior and also its effect on the axial distribution of the particle-scale dynamics remains incomplete. This is mainly because (i) in the experimental work conducted for the dense granular flow, it is difficult to measure the individual particle trajectories and the local characteristics (e.g., the collision force) due to the opacity nature and inherent complexity of the dense granular flow; and (ii) limited by computing capacity, very few numerical work tracking a large number of particles over a long time are available due to the extensive computing time required by this numerical approach. The unique behavior and pattern formation in the axial segregation process can benefit from the particle-scale simulation as the particle-scale behavior determines the macroscopic granular behavior.

Accordingly, in the current study, the parallel computation via DEM is harnessed to advance the knowledge on the axial behavioral characteristics of a binary-size mixture resulted from the size-induced axial segregation in a partially filled three-dimensional (3-D) rotating drum. Specifically, the rotating drum operates in the rolling flow regime,<sup>32</sup> which is the main operating regime in industrial applications due to its ability to provide for superior mixing and heat transfer behavior.<sup>33,34</sup> Furthermore, this regime is geometrically characterized by the coexistence of the active and passive regions in the rotating drum, which are, respectively, rapid-moving and slow-moving. Based on the simulation, the spatial evolution of the 3-D internal segregation structure is illustrated by the instantaneous distributions of the two particle types, followed by the space-time plots of the total mass, mass fraction, collision forces, and gyration radius. In addition, the axial flow directions of each particle type at different axial positions are displayed. Although the operating parameters (e.g., the drum length, rotating speed, particle properties) influence the properties (e.g., wave number and speed) of the alternating bands generated during axial segregation,<sup>2,21,35–38</sup> the current work will focus on a fixed set of conditions to shed new light on the various axial segregation phenomena.

## II. NUMERICAL METHODS AND SIMULATION CONDITIONS

In the DEM technique, the solid motion is tracked in the Lagrangian framework, i.e., each particle is tracked. The translational motion of the individual particle *i* with mass  $m_i$  is governed by Newton's second law formulated as

follows:

$$m_i \frac{dv_i}{dt} = \sum_{j=1}^k \mathbf{F}_{c,ij} + m_i \mathbf{g}, \quad (1)$$

where  $\mathbf{F}_{c,ij}$  stands for the contact force between the colliding pair and the calculation details will be discussed later;  $k$  is the total number of particles and walls colliding with the current one; and  $\mathbf{g}$  and  $t$  stand, respectively, for the gravitational acceleration and the time instant.

The rotational motion of this particle is also considered. The angular momentum balance about the center of mass of the particle  $i$  is given as

$$I_i \frac{d\omega_i}{dt} = \sum_{j=1}^k \mathbf{M}_{ij}, \quad (2)$$

where  $I_i$  and  $\omega_i$  are, respectively, the mass moment of inertia about its center of mass and rotational velocity of particle  $i$ .  $\mathbf{M}_{ij}$  is the torque generated between the colliding pair of particle  $i$  and particle  $j$ .

Due to the collision-dominated flow characteristics of dense granular flow in the rotating drum, the multiple collisions for a specific particle with its neighbouring particles frequently exist. To well capture the collision process, the soft-sphere collision model initially proposed by Cundall and Strack<sup>27</sup> to study the dense solids in the soil mechanics is adopted in the current work. Due to the deformation in the contact, the collision force between a colliding particle pair can be divided into components along the normal and tangential directions of the collision pair as

$$\mathbf{F}_{c,ij} = \mathbf{F}_{cn,ij} + \mathbf{F}_{ct,ij}, \quad (3)$$

where the subscripts  $n$  and  $t$  stand for the components of a specific variable along the normal and tangential directions, respectively. In the current work, the nonlinear collision model of Hertz–Mindlin is adopted.<sup>39</sup> The collision force between the colliding particles can be evaluated from the overlap distance and the relative velocity between them as

$$\mathbf{F}_{cn,ij} = k_{n,ij} \delta_{n,ij} \mathbf{n} + \gamma_{n,ij} \mathbf{v}_{n,ij}, \quad (4)$$

$$\mathbf{F}_{ct,ij} = \min\{(k_{t,ij} \delta_{t,ij} \mathbf{t} + \gamma_{t,ij} \mathbf{v}_{t,ij}), \mu \mathbf{F}_{cn,ij}\}, \quad (5)$$

where  $\delta_{n,ij}$  and  $\delta_{t,ij}$  represent the overlap distance along the normal and tangential directions, respectively;  $\mathbf{n}$  and  $\mathbf{t}$  are, respectively, the unit vector along the normal and tangential directions for a colliding pair.  $\mu$  is the friction coefficient of the solid phase and is used to calculate the tangential collision force using the Coulomb friction law when the slip occurs between the colliding pair.  $k_n$ ,  $k_t$ ,  $\gamma_n$ , and  $\gamma_t$  are, respectively, the normal stiffness coefficient, the tangential stiffness coefficient, the normal damping coefficient, and the tangential damping coefficient. These four parameters are related to the material properties, e.g., Young's modulus  $Y$ , the Poisson ratio  $\nu$ , and the restitution coefficient  $e$ , and can be calculated as

$$k_{n,ij} = \frac{4}{3} Y^* \sqrt{R^* \delta_{n,ij}}, \quad (6)$$

$$k_{t,ij} = 8G^* \sqrt{R^* \delta_{n,ij}}, \quad (7)$$

$$\gamma_{n,ij} = 2\sqrt{\frac{5}{6}} \beta \sqrt{S_{n,ij} m^*}, \quad (8)$$

$$\gamma_{t,ij} = 2\sqrt{\frac{5}{6}} \beta \sqrt{S_{t,ij} m^*}, \quad (9)$$

where  $\beta$  is the damping ratio ( $\beta = \frac{\ln(e)}{\sqrt{\ln^2(e) + \pi^2}}$ ).  $Y^*$ ,  $G^*$ ,  $R^*$ , and  $m^*$  are, respectively, the effective Young's modulus ( $\frac{1}{Y^*} = \frac{(1-\nu^2)}{Y_i} + \frac{(1-\nu_j^2)}{Y_j}$ ), the effective shear modulus ( $\frac{1}{G^*} = \frac{2(2+\nu_i)(1-\nu_i)}{Y_i} - \frac{2(2+\nu_j)(1-\nu_j)}{Y_j}$ ), the effective radius ( $\frac{1}{R^*} = \frac{1}{R_i} + \frac{1}{R_j}$ ), and the effective mass ( $\frac{1}{m^*} = \frac{1}{m_i} + \frac{1}{m_j}$ ) of the solid phase.  $S_n$  and  $S_t$  are, respectively, the normal and tangential stiffness and can be evaluated as  $S_{n,ij} = 2Y^* \sqrt{R^* \delta_{n,ij}}$  and  $S_{t,ij} = 8G^* \sqrt{R^* \delta_{n,ij}}$ .

In addition, the collision between the drum wall and a particle is modeled the same way as the particle-particle collision, despite assuming the wall as a sphere with an infinite mass.

Figure 1 presents the geometrical configuration of the three-dimensional horizontal cylinder containing the initial distribution of the binary-size mixture. The rotating drum has a diameter ( $D_d$ ) of 0.24 m in the transverse ( $x$ - $y$ ) plane and a length ( $L_d$ ) of 0.72 m. It rotates along its longitudinal axis (i.e.,  $z$  axis) at a rotating speed of 11.6 rpm, which corresponds to a Froude number of 0.000 457 and thereby classified as the rolling flow regime.<sup>34</sup> The radii of the small and large particles are, respectively, 3 and 6 mm and are present in equal masses that fill up 35% of the drum volume. The mixture is made up of a total of 287 660 spherical glass particles (density of 2500 kg/m<sup>3</sup>), composed of 31 962 and 255 698 large and small particles, respectively. Despite the twofold increase in the drum length here, the total number of particles may seem only slightly greater than the 226 080 of the monodisperse system investigated earlier,<sup>40</sup> but this is because the volumetric fill level is the same at 35% while the twofold increase in the particle diameter of the large particles means an eightfold increase in the volume occupied by each of these large particles. Another factor that causes the number of particles to not scale directly with the twofold increase in drum length is the increased packing of polydisperse systems relative to monodisperse ones.<sup>41</sup>

The mechanical properties of the particles adopted in the DEM simulation are listed in Table I. In our previous study on the 3-D rotating drum consisting of monodisperse particles,<sup>40</sup> qualitative and quantitative agreement with the experimental data<sup>22</sup> with respect to the angle of repose in the central and near-wall planes, the time-averaged streamwise (i.e., parallel

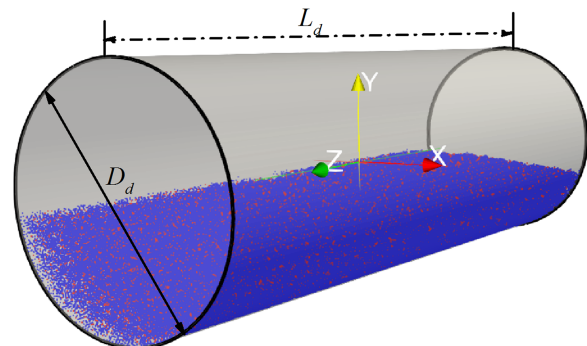


FIG. 1. Sketch of the three-dimensional rotating drum with a length of  $L_d$  and diameter of  $D_d$  with the red and blue representing the large and small particles in the initial distribution of the binary-size mixture. The Cartesian coordinate system adopted in this study is such that the origin is in the drum center, the  $y$ -direction is opposite to that of the gravitational force, and the  $x$  and  $z$  directions are perpendicular and parallel to the drum length, respectively.

TABLE I. Mechanical properties of the solid phase adopted in the DEM simulation.

Young's modulus (Pa)	$1.0 \times 10^8$
Poisson ratio	0.24
Restitution coefficient of particle-particle collision	0.97
Restitution coefficient of particle-wall collision	0.85
Friction coefficient of particle-particle collision	0.30
Friction coefficient of particle-wall collision	0.35

to the particle bed surface) velocity, and the active layer thickness demonstrates the validity of the numerical algorithm and the numerical parameters. In the current study, the validation carried out in our previous study<sup>40</sup> is expected to hold, since the drum radius and solid material are the same, except that the drum length is enlarged twofold along the  $z$ -direction and the particle size distribution is bidisperse. Regarding the drum length, its size is expanded twofold to mitigate the end wall effects on the band formation but not any larger in view of the computational time.

Since the first axial band induced by axial segregation typically occurs near the end walls on the order of  $10 \sim 100$  revolutions of the rotating drum<sup>21</sup> (note that the rotating speed is 11.6 rpm, which means 5.17 s/revolution), a total of 280 physical seconds (i.e., 54 revolutions) is simulated with a combination of  $4 \times 1 \times 8$  CPUs in parallel along the  $x$ ,  $y$ , and  $z$  directions, respectively, to speed up the simulation. It should be noted that there still exists band coarsening and oscillation over a much longer time scale on the order of 1000 revolutions.<sup>42</sup> However, that is not considered in the current work, which focuses on band formation, in order to shed some light on the interplay between the dynamical evolution of axial segregation and the initial band growth.

### III. RESULTS AND DISCUSSION

#### A. Dynamic segregation behavior of the solid phase

Due to the opaque nature of the granular material, it is cumbersome to observe the internal segregation structure of the solid phase. However, numerically tracking the solid motion makes it possible. Figure 2 presents the 3-D illustration of the instantaneous particle distribution of the large and small particles in the rotating drum. Each row represents the internal segregation structure at each time instant evaluated (namely, 4, 10, 20, 40, 140, and 280 s). The instantaneous distributions of the large and small particles, respectively, coloured with the red and blue are presented in the first column. The second column illustrates the demarcation of the regions dominated by each particle type. Specifically, the red and blue iso-surfaces represent the boundaries whereby the mass fractions of, respectively, the large and small particles are 0.6. To calculate the mass fraction, the whole rotating drum is enclosed by a cubic box and divided into cubic cells of 6 mm on each side, after which the mass fraction of each particle type is evaluated. Regarding the size of the cubic cell, it should be small enough for sufficient spatial resolution, while large enough to enclose more particles. In the current work, in view of the twofold difference in particle sizes, the mass fraction in each cell was evaluated for many samples over a short time interval to ensure

that the statistical results are independent of the cell size. Figure 2 illustrates the differences in the segregation behavior of the two particle types. At the time instant of 4 s [Figs. 2(a) and 2(b)], the radial segregation due to the kinetic sieving<sup>43</sup> effect results in the large particles dominating the peripheries of the rotating drum [Fig. 2(b)] and small particles in the radial core, while the axial segregation is not obvious yet. At the time instant of 10 s [Figs. 2(c) and 2(d)], the proportion of small particles distributed at the bed surface is less [Fig. 2(c)], and the end wall region displays a clear radial segregation of large and small particles, respectively, away from and towards the radial core [Fig. 2(c)]. At the time instant of 20 s, the radial segregation becomes clearer, with large particles dominating the outer radial positions of the rotating drum [Fig. 2(e)], and the jagged iso-surfaces indicating the well-mixed regions interspersed with the segregated regions [Fig. 2(f)]. Signs of axial segregation can be seen at the end wall in Fig. 2(e) in terms of a larger proportion of large particles, which is caused by the friction with the end walls.<sup>17</sup> Then at the time instant of 40 s [Figs. 2(g) and 2(h)], the radial profiles are approximately similar to that at the time instant of 20 s [Figs. 2(e) and 2(f)], which indicates that the radial segregation has nearly finished within seven revolutions. At this time, the axial segregation starts to become more apparent, as seen in the appearance of axial bands of small particles at the bed surface in Fig. 2(g). The preferential segregation of the large particles at the end walls causes the small particles to move away from the end walls, which thereby form two axial bands of predominantly small particles. At the time instant of 140 s [Figs. 2(i) and 2(j)], the end walls are dominated by large particles and two axial bands dominated by small particles appear near the end walls. At the last time instant evaluated at 280 s [Figs. 2(k) and 2(l)], the axial bands become slightly more dominated by small particles than that at 140 s [Figs. 2(i) and 2(j)], which indicates that the axial segregation is slow. Therefore, the numerical results presented in Fig. 2 dynamically capture the initial fast radial segregation and then the slow axial segregation and even the band formation of different particle types in the rotating drum.

#### B. Space-time plot of mass distribution along the drum length ( $z$ -direction)

The axial segregation leads to the re-distribution of both particle types along the axial direction, leading to the formation of axial bands consisting mainly of one particle type and also the re-distribution of the total mass along the drum length. Since the total mass is a macroscopic property of the drum, the question addressed here is whether it is a global parameter that is not influenced by the segregation phenomenon, as is the case for the total kinetic energy of all the particles.<sup>44</sup> Experimentally probing the re-distribution of solid mass along the axial direction is hard to achieve, and thus no information regarding the effect of granular axial segregation on the mass distribution has been reported earlier. However, tracking all the particles using particle-scale simulation makes this kind of study possible. Figures 3(a)–3(c) illustrate the space-time plots of axial mass distribution of, respectively, all particles, large particles, and small particles, which are obtained by dividing the drum length (0.72 m) into 36 equal transverse ( $x$ - $y$ ) slices then summarizing

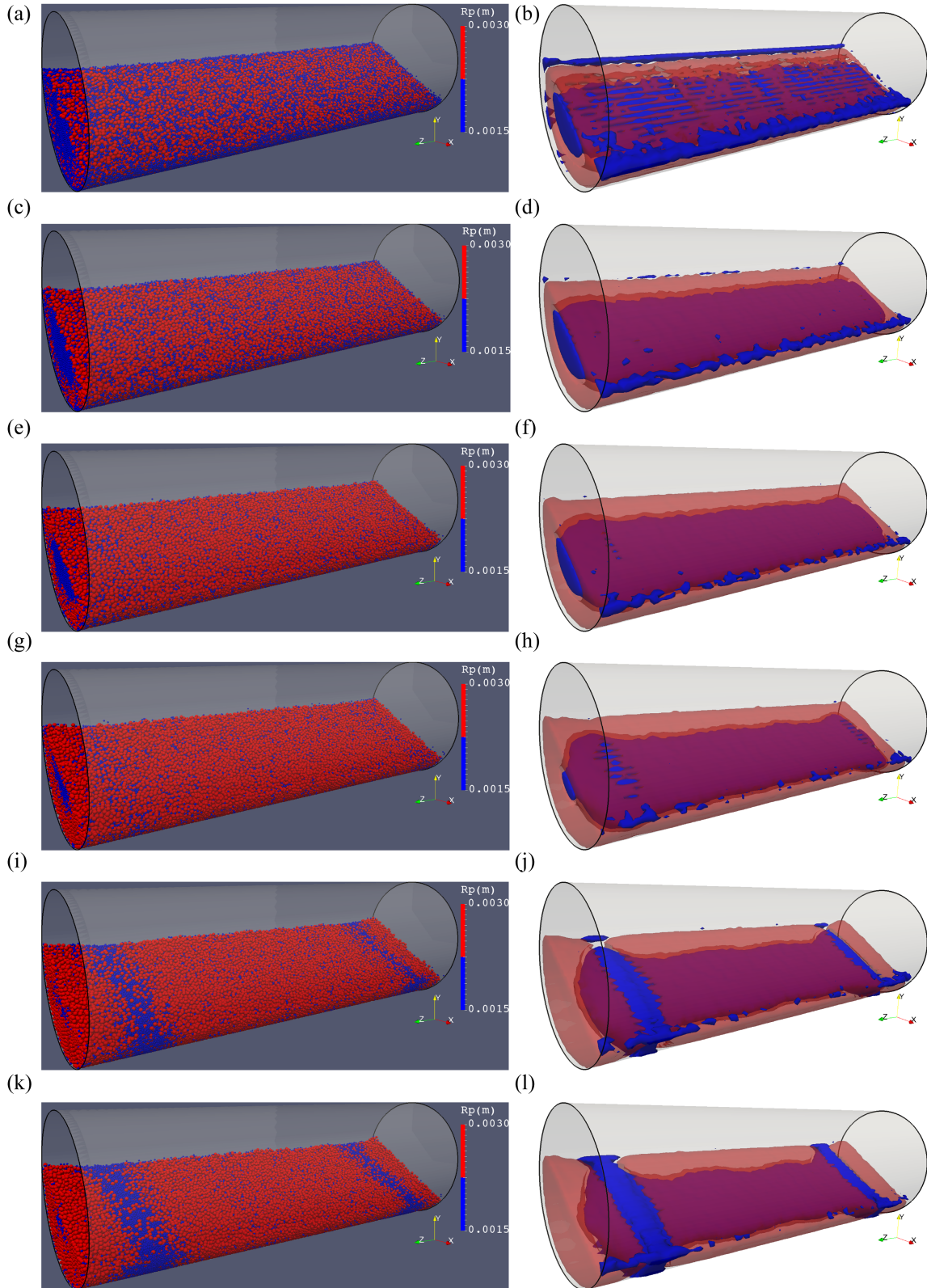


FIG. 2. 3-D illustration of the dynamic segregation behavior of the solid phase in the rotating drum at various time instances. The first column depicts the instantaneous distributions of the solid phase, with the red and blue particles representing the large and small particles, respectively. The second column depicts the internal segregation structure of the two particle types. Specifically, the red and blue iso-surfaces represent the positions where, respectively, the large and small particles have a mass fraction of 0.6. (a)  $t = 4$  s, (b)  $t = 4$  s, (c)  $t = 10$  s, (d)  $t = 10$  s, (e)  $t = 20$  s, (f)  $t = 20$  s, (g)  $t = 40$  s, (h)  $t = 40$  s, (i)  $t = 140$  s, (j)  $t = 140$  s, (k)  $t = 280$  s, (l)  $t = 280$  s.

the mass of the related particles in each slice. Note that the slices of  $z/Z = \pm 1$  and 0 correspond to the axial planes at the end walls and axial center, respectively. Furthermore, Fig. 3(d)

displays the changes of total mass with time in the regions closer to the end walls ( $0.78 < |z/Z| < 1$ ) and also at the axial center region ( $|z/Z| < 0.055$ ). The symmetrical behavior

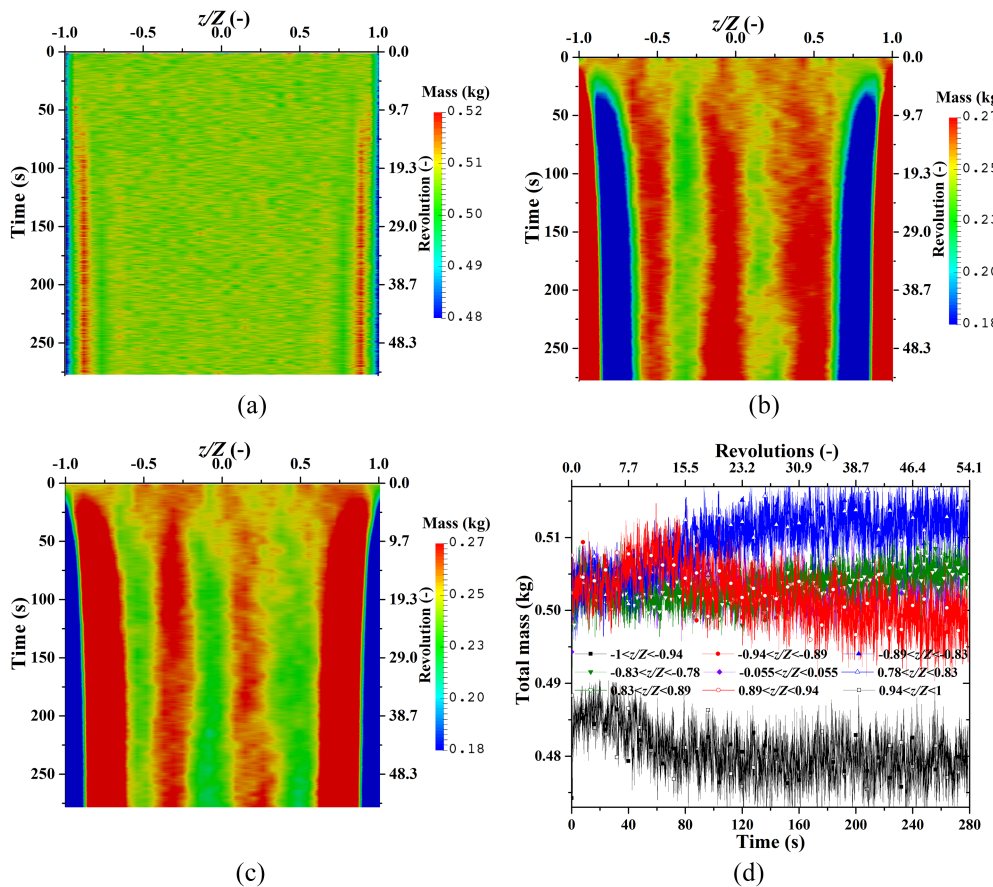


FIG. 3. Space-time plots of total mass of all the particles (a), mass of large particles (b) and small particles (c) in the rotating drum along the drum length, in which  $z$  and  $Z$  are, respectively, the axial position assessed and the half-length of drum length, whereby  $z/Z = \pm 1$  and 0 represent the end walls and axial center, respectively; and (d) evolution of the total mass of the solid phase in the region  $0.78 < |z/Z| < 1$  and the central region  $|z/Z| < 0.055$ , with solid and open symbols of the same kind standing for, respectively, the negative and positive  $z/Z$  positions.

about the axial center is clear in Fig. 3. Figures 3(a)–3(c) show that the steeper changes in the axial mass distribution with time occur within 100 s (nearly 19.4 revolutions), after which the changes are gradual with respect to time. This indicates that the axial distribution of total mass of solid phase is not a global parameter but obviously influenced by the inherent axial segregation. During the initial period ( $t < 4$  s), the mass distribution is approximately uniform along the drum length [Fig. 3(a)]. This is because the kinetic sieving only gives rise to the solid redistribution in the transversal plane but does not affect the axial mass distribution. During  $t = 4\text{--}40$  s, the total mass near the end walls ( $z/Z \sim -1$ ) decreases due to friction with the end walls during the initial onset of axial segregation. At about  $t = 40$  s, the increased total mass at  $0.83 < |z/Z| < 0.89$  [Fig. 3(a); and quantified in Fig. 3(d)] is due to the decreased interstitial voids associated with a mixture of both particle types (due to the small particles percolating through the interstices of the large particles); Fig. 6 further illustrates this. Specifically, the two streaks of higher mass in the space-time plot in Fig. 3(a) correspond to the intermediate region in between the alternate bands of the two particle types near the end walls, i.e., axial band of large particles at the end wall, followed by axial band of small particles. From  $t = 40$  s onwards, as axial segregation progresses, the axial mass distribution is relatively constant with time. It is evident from Figs. 3(a) and 3(d) that the mass distribution of all the particles in the

parts away from the end walls (i.e.,  $|z/Z| < 0.78$ ) of the rotating drum is approximately constant for the entire duration investigated, which indicates the limited effects exerted by axial segregation on the packing density of the particles in the central part of the drum. In contrast to the total mass distribution of all the particles [Fig. 3(a)], the axial mass distributions of large [Fig. 3(b)] and small [Fig. 3(c)] particles are not as uniform due to the formation of the alternate axial bands of large and small particles along the drum length. Specifically, five axial bands of large particles [evident in Fig. 3(b) as greater mass] can be observed in the regions  $|z/Z| \sim 1, 0.5$ , and 0, while four axial bands of small particles [evident in Fig. 3(c) as greater mass] appear in the regions of  $|z/Z| \sim 0.25$  and 0.75. The axial bands nearest to the end walls of large and small particles exhibit the boldest colors due to the most significant influence of friction with the end walls. Furthermore, it should be highlighted that the number of bands of both particle types will not be constant with time but display a logarithmic decay due to the band coarsening effect over a period of the order of thousands of drum revolutions.<sup>21,25</sup>

### C. Mass fraction distribution of the two particle types

As compared with the other particle-scale parameters, mass fraction is a key parameter representing the axial segregation dynamics and has been commonly reported in

several experimental efforts focused on axial segregation,<sup>30,31,45</sup> band number and travelling speed,<sup>21</sup> and coarsening dynamics.<sup>38,46</sup> In the rotating drum studied here, the initial homogeneous binary-size mixture is such that the large and small particles are of equal mass, so regions with mass fractions of large particles of greater than 0.5 indicate regions where the large particles have preferentially congregated. Figure 4 presents the space-time plots of the mass fraction of large (a) and small (b) particles across the drum length (i.e.,  $z/Z$ -direction). In view of the closely tied relationship, the following discussion is mainly focused on the mass fraction distribution of the large particles. The axial segregation induced by the wall friction leads to the accumulation of large particles near the end wall especially in the first 25 s, which is due to the onset of the axial band. Simultaneously, the band with small particles appears and becomes apparent especially after 50 s. Subsequently, with the continuous axial segregation, these bands near the end wall become wider in the period before 200 s [quantitatively illustrated in Fig. 5(a)], which is due to the continuous accumulation of particles in the axial bands. After that, the bandwidths of large and small particles near the end wall are nearly constant, indicating that the segregation process in this part is almost saturated. Two trends in Fig. 4 are clearly in contrast to that implied by the total mass distribution in Fig. 3(a). First, the axial segregation starts when drum rotation starts ( $t = 0$  s), instead of after the achievement of radial segregation as implied by the total mass distribution in Fig. 3(a). Specifically, during the initial period ( $t < 4$  s), the higher mass fraction of large particles at the end wall ( $z/Z \sim 1$ ) is obvious, which indicates that the end walls immediately induces the axial segregation via friction. This observation

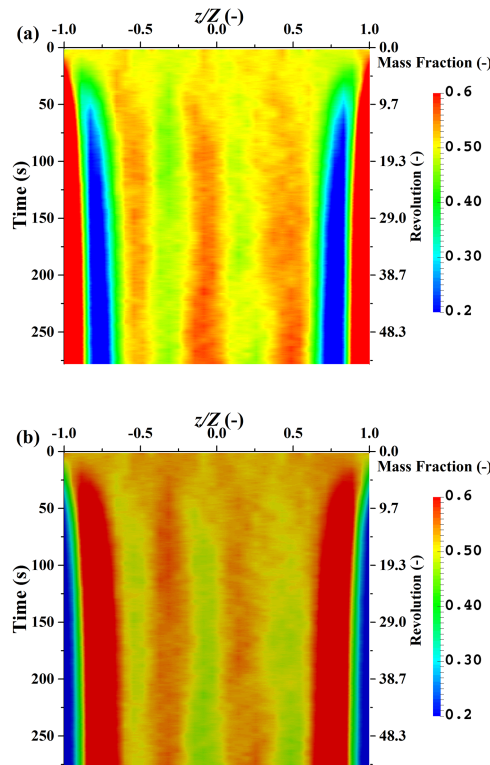


FIG. 4. Space-time plots of the mass fraction of large (a) and small (b) particles across the axial length of the rotating drum.

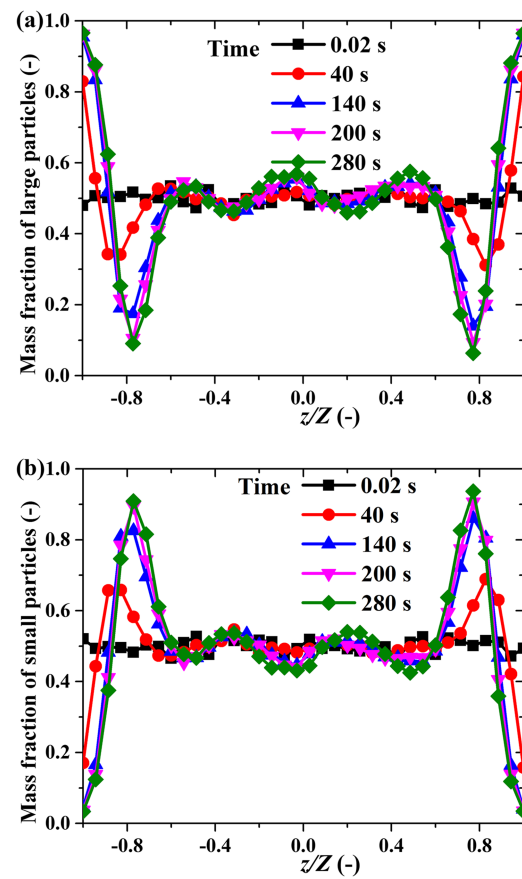


FIG. 5. Comparison of the axial distribution of the mass fraction of large (a) and small (b) particles at several time instants.

provides a surprising insight into the relationship between radial and axial segregation, for which the previous work has claimed that the axial segregation must always be preceded by radial segregation<sup>2,18</sup> and also the radial segregation is necessary for the axial segregation.<sup>2</sup> Second, three bands of a higher mass fraction of large particles appear in the axial center of the drum (i.e.,  $z/Z \sim -0.5, 0, 0.5$ ), which can also be observed in Figs. 2(l), 3(b), and 5(a). However, the extent of size-segregation is lesser compared with that near the end walls, as evident in the lower mass fractions associated with these bands compared with that at the end walls. The formation of these axial bands at the axial center is extremely slow relative to that near the end walls, which is mainly due to the diminished influence of the end walls. In previous experimental reports, the axial bands far away from end walls appear after tens of thousands of revolutions,<sup>24,25,48</sup> which is beyond the time span simulated via DEM here. Also, it should be noted that band dynamics (e.g., wavelength and growth-rate) have been previously reported to be influenced by the operating parameters (e.g., drum diameter and length).<sup>35,47</sup>

To quantify the axial segregation of the system, Fig. 5 presents the axial distribution profiles of the mass fraction of large (a) and small (b) particles at several time instants. Four observations related to the axial segregation can be observed. First, the size segregation is most extensive near the end walls, with drastic increases and decreases of the mass fractions of, respectively, the large and small particles until about  $t = 140$  s.

Specifically, the axial bands of large and small particles near the end walls are at  $|z/Z| > 0.89$  and  $0.66 < |z/Z| < 0.83$ , respectively. After 140 s, the change with time is more gradual, indicating the saturation of the bands. Second, between  $t = 140$  and 280 s, slight changes are observed in the profiles, which indicate that axial segregation continues but very slowly. Third, in the central part of the drum ( $|z/Z| < 0.6$ ), several bands of large and small particles appear as indicated by the peaks in Figs. 5(a) and 5(b), respectively. The magnitudes of the peaks increase with time due to the slower congregation of the specific particle type in the bands. Fourth, the peaks move slightly axially with time, which correspond to the band oscillation and wave dynamics of the axial band, as has been previously reported.<sup>48,49</sup>

To quantitatively describe the variation of the mass fraction of large particles along the drum length with time, Fig. 6 presents the profiles of the evolution of the mass fraction of large (a) and small (b) particles in the  $|z/Z|$  range of 0.78 and 1, and the central region ( $|z/Z| < 0.055$ ). As expected, the mass fractions of both the large and small particles are symmetrical about the axial center of the drum. The trends of the large particles are opposite to that of the small, and thus the following discussions are mainly carried out based on the mass fraction of large particles. Three observations are worth highlighting. First, it should be mentioned that the continuous axial transportation of the solid phase exists especially for the central

region  $|z/Z| < 0.055$ , which is mainly due to the dynamical evolution of granular material over a long time scale, e.g., the time scale for band coarsening is nearly on the order of 1000 rotations.<sup>29</sup> In this part, the mass fraction of large particles increases slowly, which as discussed in the axial mass [Fig. 3(b)] and mass fraction [Fig. 4(a)] trends. Second, it is only in the regions closer to the end wall ( $|z/Z| > 0.83$ ) that the mass fraction of large particles is greater than 0.5, which indicates the preferential segregation of large particles to this region. The highest concentration of large particles is in the region closest to the wall ( $|z/Z| > 0.94$ ), at which the mass fraction of large particles increases steeply initially ( $t < 40$  s) in this process and then gradually approaches nearly 1, demonstrating the saturation status of large particles here. As for the regions slightly away from the wall ( $0.83 < |z/Z| < 0.94$ ), the mass fraction of large particles decreases before increasing, the initial decrease of which is due to the strong tendency for the large particles to preferentially segregate to the end wall ( $|z/Z| > 0.94$ ) initially. Third, instead of the mass fraction of the large particles decreasing monotonically with distance from the end wall, a non-monotonic trend is observed, specifically in that the mass fraction of large particles decreases then increases with  $z$  in the range of  $0.78 < |z/Z| < 0.83$ . Details regarding the directional flow of large and small particles will be discussed below to explore further the mechanisms underlying the segregation phenomenon.

#### D. Space-time plot of collision force exerted on large and small particles

In the rotating drum, other than gravity, the collision force arising from particle-particle and particle-wall collisions is the only other dominant force exerted on the solid phase. While the gravity only acts in a single direction ( $y$ ), the collision force dictates the movement of particles in all directions, hence warrants a more in-depth inspection to understand the segregation behavior. It is extremely hard to obtain the contact force in the experiment, whereas the particle-scale simulation provides an effective approach to explore the effect of axial segregation on the contact force. The space-time plot of the non-dimensionalized collision force exerted on the small and large particles along the drum length is presented in Fig. 7. Specifically, the non-dimensionalized force exerted on each particle type is obtained by dividing the collision force by the gravitational force of each particle of the same type, then spatially averaged across the axial region assessed. The first column represents the large particles, while the second for the small particles. Note that the range on the scales for the large particles (first column in Fig. 7) is less than half of that exerted on the small particles (second column in Fig. 7). The first, second, and third rows represent the collision forces experienced by two particle types along the directions  $x$ ,  $y$ , and  $z$ , respectively. Note that, for the small particles, the range of  $F_y'$  [Fig. 7(d)] is greater than that of  $F_x'$  [Fig. 7(b)] and  $F_z'$  [Fig. 7(f)] because of the influence of gravity in the  $y$ -direction and setting to the same range would obliterate the variations. Consistent with the earlier figures, the most drastic changes occur initially, and then the changes become very gradual with time. Four interesting observations are listed as follows: First, regardless of the particle type and direction, the non-dimensionalized

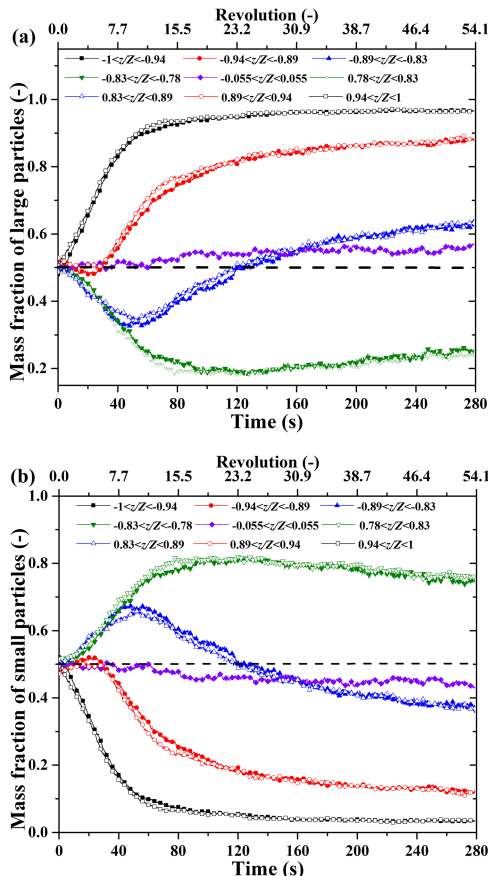


FIG. 6. Evolution of the mass fraction of large (a) and small (b) particles in the near-wall region  $0.78 < |z/Z| < 1$ , and the central region  $|z/Z| < 0.055$ , with solid and open symbols of the same kind standing for, respectively, the negative and positive  $z/Z$  positions.

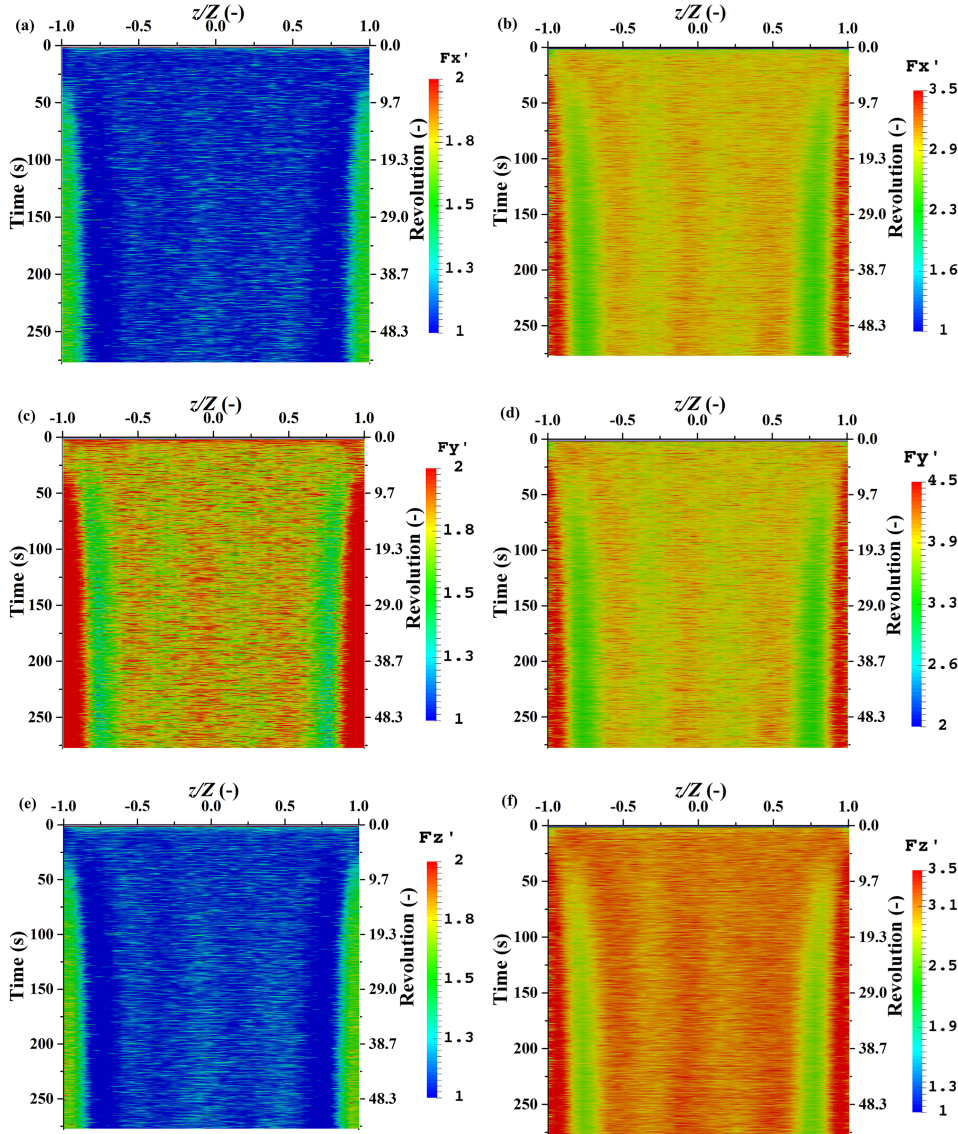
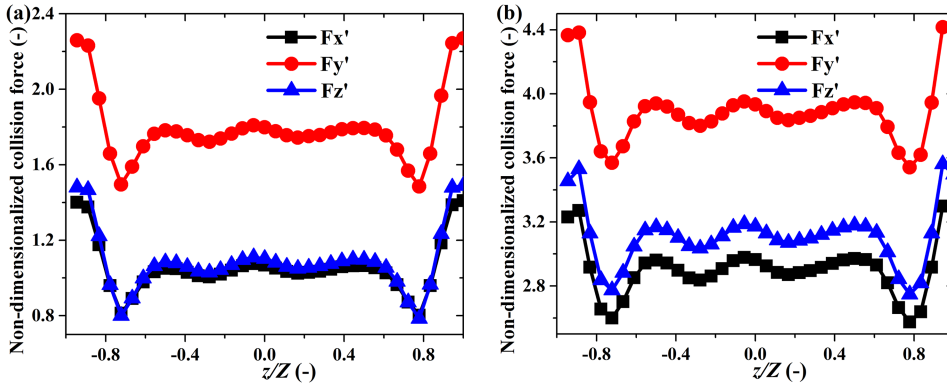


FIG. 7. Space-time plot of the non-dimensionalized collision force (i.e., collision force normalized with gravitational force) exerted on small and large particles along the drum length in all three directions: (a)  $F_x'$  of large particles; (b)  $F_x'$  of small particles; (c)  $F_y'$  of large particles; (d)  $F_y'$  of small particles; (e)  $F_z'$  of large particles; and (f)  $F_z'$  of small particles.

collision forces are the greatest at the end walls ( $z/Z \sim 1$ ). This may be due to two reasons: (i) the presence of the additional particle-wall collision; and (ii) the larger interstices between the neighbouring particles due to fewer small particles lead to a vigorous collision between particles. Second, regarding the formation of the axial bands near the wall at approximately  $|z/Z| \sim 0.8$  also seen earlier in Figs. 3(a) and 4, the bands manifest as distinctly lower non-dimensionalized collision forces in all three directions for both particle types. Third, the size-induced axial segregation leads to a gradual change with time [e.g., increased  $F_x'$  of large particles when the band formed near the end walls, as shown in Fig. 7(a)] of the collision force experienced by these two particle types and thus a non-uniform distribution along the drum length. Meanwhile, the region with large collision force coarsens in the same trend as with the mass fraction distribution shown in Fig. 4. The lower magnitudes of collision force exerted on both particle groups are likely linked to the increased concentration of small particles (Fig. 4). Interestingly, although higher collision forces are associated with small particles [Figs. 7(b), 7(d), and 7(f)] compared with large particles

[Figs. 7(a), 7(c), and 7(e)], bands with predominantly large particles at the end walls exhibit higher collision forces for both particle types. The axial segregation presumably increases the collision forces in the regions with more large particles; more understanding beyond the scope of the current study is needed to shed light on this.

The band formation in the axial segregation is fast, and thus no apparent change of the particle-scale information driving the pattern evolution can be vividly observed. To quantitatively compare the collision force exerted on the different particle types, Fig. 8 presents the axial distribution of the time-averaged non-dimensionalized collision forces in all three directions along the drum length exerted on the large [Fig. 8(a)] and small [Fig. 8(b)] particles. In general, the axial segregation of the solid phase along the  $z$  direction leads to the non-uniform distribution of the collision force of both particle types along this direction. Axially, the highest non-dimensionalized collision forces are at the end walls ( $|z/Z| \sim 1$ ) due to the additional particle-wall collisions, while the lowest is associated with the axial bands at  $|z/Z| \sim 0.75$ . Among the directions, the  $x$ - and  $z$ -directional components are more similar. Furthermore, the



$y$ -directional non-dimensionalized collision force ( $F_y'$ ) are the greatest for both particle types, which is mainly due to the two aspects: (i) in the uplifting process, the collision force has to overcome gravity; (ii) in the rapid falling process in the active region, the gravity accelerates the falling flow that leads to vigorous collision between the particles. Between the two particle types, the collision force exerted on the small particles is significantly greater than that on the large particles along all three directions, which may further influence the dispersion of these two particle types along the axial direction. Specifically, although it has been widely accepted that the end wall induces the axial segregation, the in-depth understanding of this mechanism is still needed. By exploring the collision force, it should be highlighted that the collision force exerted on the small particles near the end wall is obviously larger than that on the large particles, which may be the source for the axial segregation in this period.

### E. Flow patterns in the transverse ( $x$ - $y$ ) planes along the drum length

The axial segregation induced by the end walls leads to the axial movement of the particles, which leads to distinctive distributions of the different particle types in the axial direction. Such axial movement is inextricably linked to the axial segregation trends. However, whether there is a preferential region of the axial motion of each particle type at each axial position is a question that has not been addressed before. Hence a closer look is worthwhile. Figure 9 presents the scatter plots of all the large and small particles crossing the  $x$ - $y$  slice at  $z/Z = -0.89$ , where axial segregation is extensive, over the whole simulation duration of 280 s. Specifically, each discrete data point represents the exact position at which a specific particle of each type crosses the targeted plane of  $z/Z = -0.89$  at each time instant, while each green line stands for the active-passive interface.

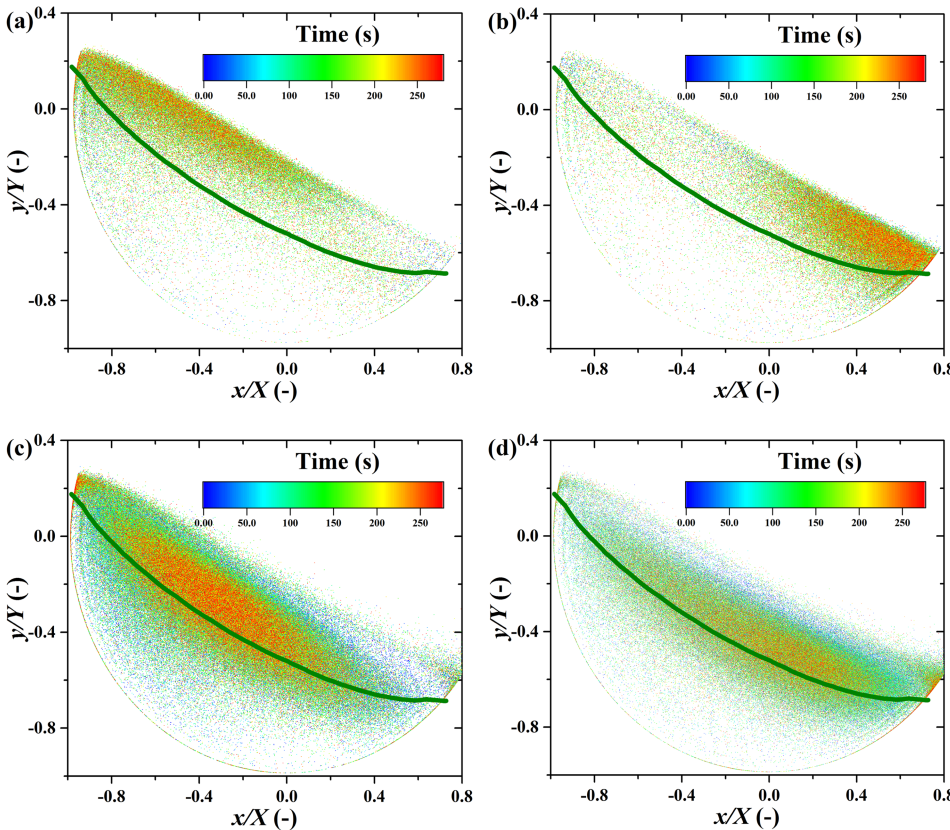


FIG. 9. Scatter plot of the positive and negative axial motion of particles in the  $x$ - $y$  slice at  $z/Z = -0.89$  over the whole simulated duration of 280 s: (a) axial flow of large particles towards axial center; (b) axial flow of large particles towards the end wall ( $z/Z = -1$ ); (c) axial flow of small particles towards axial center; and (d) axial flow of small particles towards the end wall ( $z/Z = -1$ ). Each discrete data point represents one particle detected in the specific direction, while each green line stands for the active-passive interface.

interface. The top and bottom rows represent, respectively, the large and small particles, while the left and right columns represent, respectively, the movement towards the axial center ( $z/Z = 0$ ) and end wall ( $z/Z = -1$ ). With respect to the particle type, the similarities are that the axial flow predominantly is in the active region for both particle types in both directions and spans the same  $x/X$  ranges in each direction. On the other hand, the difference between the particle types lies in that the large and small particles dominate, respectively, the portion nearer the bed surface and nearer to the active-passive interface portions within the active region. Apparently, this is tied to the fast radial segregation as this process is achieved within several revolutions. Regarding the flow direction, the particles tend to move towards the axial center at the higher  $y/Y$  positions, whereas towards the end walls at the lower  $y/Y$  positions, with this tendency being more obvious as the slow axial segregation progresses, especially in the period after 200 s. The most important insights on the axial flow behavior are that (i) the axial flow of both particle types in both directions are observed, which indicates the dynamic axial exchanges; (ii) the axial flow of both particle types towards the axial center is more dominant at the higher  $y/Y$  positions, which is due to the effect of the friction induced by the cylindrical wall to lift the particles from the passive region to the active one; and (iii) the axial flow of large particles exhibits higher probabilities near the two ends of the active region due to the preferential radial segregation of the large particles away from the radial core.

Analogous to Fig. 9, Fig. 10 displays the scatter plots for an  $x$ - $y$  slice further from the wall, namely,  $z/Z = -0.44$ . Similar to Fig. 9, Fig. 10 shows that (i) both particle types move

in both axial directions; and (ii) the large particles dominate closer to the bed surface while the small ones tend towards the radial core due to the radial segregation. In contrast to Fig. 9, Fig. 10 indicates that (i) the data points are scattered over a wider area, particularly with the small particles spreading across almost the entire particle bed, demonstrating that the mixture of particle types still exists despite radial segregation [as can be observed from Fig. 2(k)] such that small particles occasionally appear in the radial periphery; (ii) the two directions exhibit similar trends for the same particle type, which suggests the random axial motion; (iii) the preferential regions of the points crossing this plane mainly lies in the radial core and periphery for the small and large particles, respectively. While the scatter plots representing the flow directions towards and away from the end walls are clearly different for each particle type at about 5% of the drum length away from the end wall (Fig. 9), the scatter plots representing the two directions are similar at approximately 25% of the drum length away from the end wall (Fig. 10). This indicates that the end wall effects on the axial flow direction are limited to a short axial distance from the end walls.

To further explore the axial flow behavior, Fig. 11 presents the vector plots of the time-averaged solid velocity ( $U_s$ ) in two slices parallel to the bed surface. Figure 11(a) represents the bed surface, while Fig. 11(b) represents the slice 0.03 m below and parallel to the bed surface. The solid flow in these two slices is regular in terms of the general downward motion of the particles. Compared with the bed surface [Fig. 11(a)], the velocities in the lower slice [Fig. 11(b)] are slower. A closer look particularly of the bed surface [especially Fig. 11(a)] indicates that the velocity vectors near the end walls have an axial component,

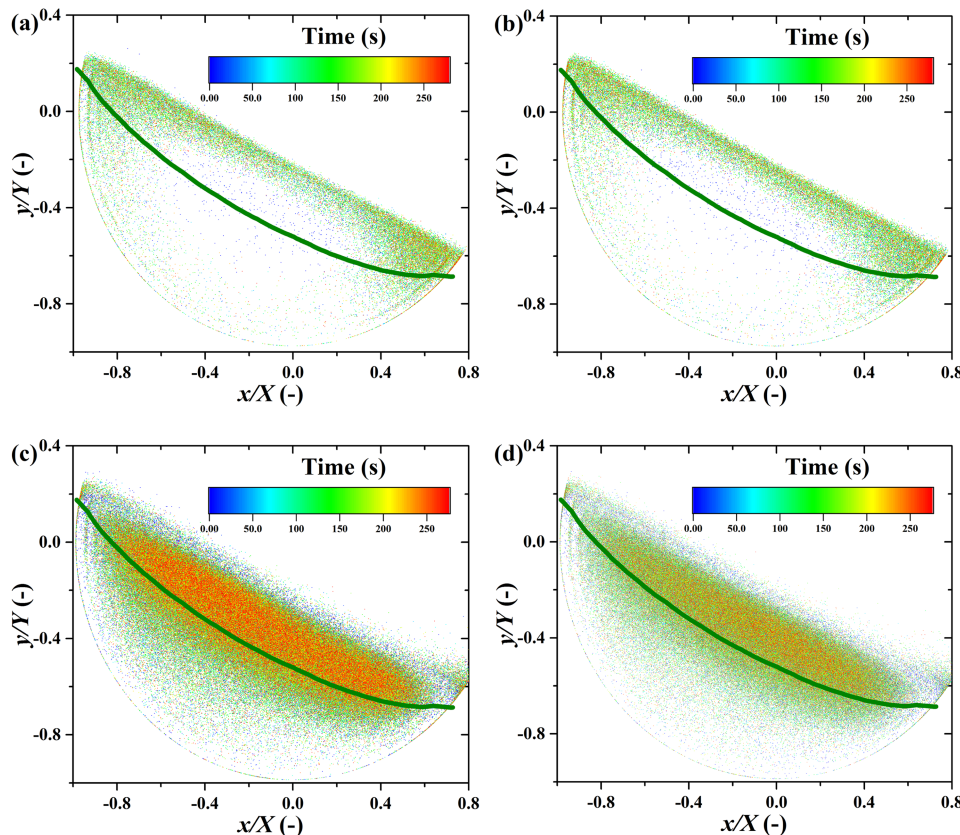


FIG. 10. Scatter plots of the positive and negative axial motion of particles in the  $x$ - $y$  slice at  $z/Z = -0.44$  over the whole simulation duration of 280 s: (a) axial flow of large particles towards axial center; (b) axial flow of large particles towards the end wall ( $z/Z = -1$ ); (c) axial flow of small particles towards axial center; and (d) axial flow of small particles towards the end wall ( $z/Z = -1$ ). Each discrete data point represents one particle detected in the specific direction, while each green line stands for the active-passive interface.

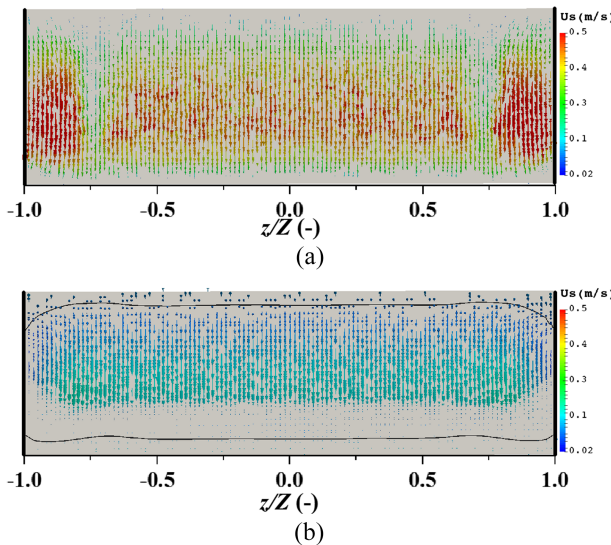


FIG. 11. Vector plots of the time-averaged solid velocity ( $U_s$ ) in two slices parallel to the bed surface: (a) bed surface and (b) slice at a distance 0.03 m lower than and parallel to the bed surface. The black line represents the active-passive boundary.

which is different from those in the central part. Specifically, some trajectories around the axial bands tend towards the axial center in the top half of the slice (higher  $y/Y$  positions) and towards the end walls in the bottom half of the slice (lower  $y/Y$  positions), which results in the axial flow of both particle types towards and opposite to the end wall in the lower and upper regions, respectively. This agrees with the directional flow discussed in Fig. 9. The axial flow behavior of both particle types is because the friction induced by the end walls causes the particles to be lifted up from the passive region to move towards the axial center at the higher  $y/Y$  positions, which thereby causes the particles in the lower  $y/Y$  positions to move towards the wall to abide by the mass conservation principle. Especially in the region near the end wall, no obvious axial flow of solid phase in the active region is observed, which is mainly due to the negligible effect of end wall on the axial behavior here. Thus, the axial flows of both the large and small particle types behave similarly towards and opposite from the end wall in both the active and passive regions, as discussed in Fig. 10.

## F. Space-time plot of the gyration radius

In a well-mixed system, the mean gyration radius (defined as the distance between a specific particle and the rotating axis) of different particle types should be the same. However, the radial and axial granular segregation phenomena lead to evolving axial distributions of gyration radii of the two particle types in a binary mixture. Figures 2 and 3 have shown that the small particles preferentially segregate radially and axially to the core of the particle bed, with the radial segregation occurring quicker than the axial one. To further understand the evolution of the rotating behavior of the granular material, the axial distribution of the gyration radii of different particle types needs to be assessed. The gyration radius of the particles of different sizes is a direct result of radial segregation, which causes the small and large particles to preferentially

segregate, respectively, to the radial core and radial periphery. Because the different gyration radii mean that particles rotate at the different radial positions, the preferential region for the axial motion of the different particle types is affected as well (as discussed in Figs. 9 and 10). The gyration radii at each axial position at each time instant presented here are obtained by dividing the rotating drum into 36 equal parts along the  $z$ -direction, then averaging the gyration radii of each particle type across the  $x$ - $y$  slice. Figures 12(a) and 12(b) illustrate the space-time plots of the average gyration radius ( $L$ ) with respect to the drum length ( $z$ ) for, respectively, the large and small particles up to 280 s. In the first 40 s, due to the dominance of the fast radial segregation, Fig. 12 indicates that the gyration radii of the large and small particles, respectively, increases and decreases uniformly across the drum length, due to the preferential segregation of the large particles to the radial periphery and small particles to the radial core. Expectedly, as the gyration radius of one particle type increases, that of the other has to decrease to fill the space. As time progresses, the slow axial segregation becomes apparent, which causes the axial bands to form. At  $t \sim 40$  s, the gyration radii of the large particles near the end walls gradually decrease because the band formation of large particles gives rise to more particles located in the core region and thus macroscopically lowers the gyration radii in this part. Meanwhile, with the bandwidth increasing, the decreasing tendency moves towards the center due to the enlarged width of this band (Fig. 5). For the gyration radii of

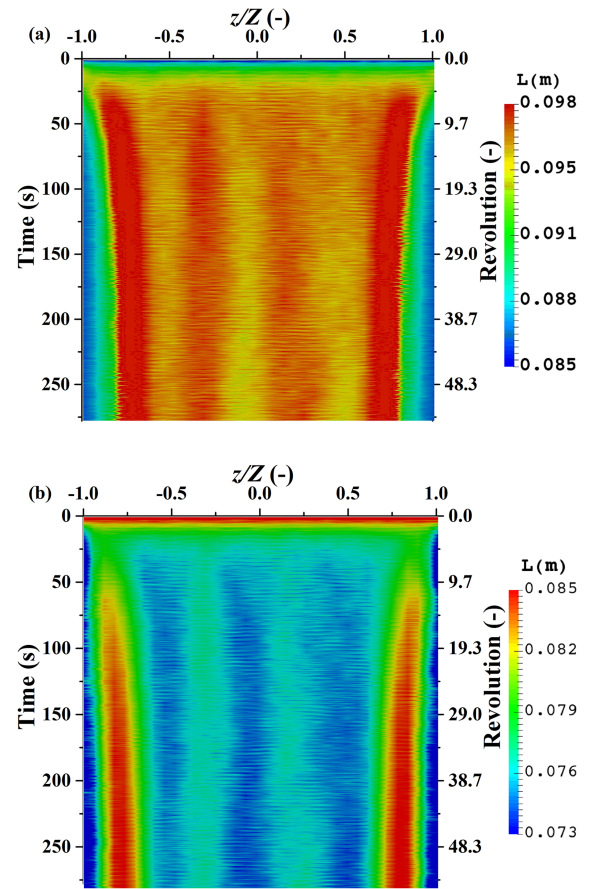


FIG. 12. Space-time plot of the gyration radius ( $L$ ) with respect to the drum length of the two particle types: (a) large particles and (b) small particles.

small particles [Fig. 12(b)], the band formation for the large particles near the end wall leads to the leave of small particles in this region and thus obvious lower gyration radii of small particles can be obtained. In the band of small particles, the gyration radii enlarge gradually especially after 60 s, which is mainly because the band formation of small particles gives rise to more and more small particles concentrating in the periphery of this part, as clearly demonstrated in Fig. 2. From  $t \sim 40$  s onwards, the positions of  $-0.6 < z/Z < 0.6$  exhibit alternating bands of lower and higher gyration radii, specifically such that a band displaying lower gyration radii of the large particles corresponds to higher gyration radii of the small particles, and vice versa, as reflected in Fig. 2(g) and 2(l), obviously indicating that the band formation changes the gyration radii of different particle types.

Figure 13 quantifies the evolution of the axial gyration radius profiles for the large (a) and small (b) particles in the range of  $|z/Z|$  of 0.78–1, and the central region of  $|z/Z| < 0.055$ . Each gyration radius is a spatial average of all the particles of this type in the corresponding region assessed. For the large particles [Fig. 13(a)], the gyration radii increase steeply in the  $z/Z$  range investigated in the first 15 s, which indicates

that the large particles preferentially segregate radially to the radial periphery initially. Correspondingly, in the first 15 s for the small particles [Fig. 13(b)], the gyration radii decrease steeply with time for the  $z/Z$  positions investigated, to fill the space vacated by the preferential segregation of the large particles. Subsequently, for  $t > 15$  s, the axial segregation obviously affects the gyration radii of large [Fig. 13(a)] and small [Fig. 13(b)] particles, (i) in the region far from the end wall ( $|z/Z| < 0.055$ ), the gyration radii of both the large and small particle types change the least, which is mainly due to the negligible effect of the end wall on this region; (ii) in the region near the end wall ( $|z/Z| > 0.78$ ), the increase over the next few seconds before the decrease of the gyration radii of large particles is in accordance with the radial segregation and band formation process. Correspondingly, the gyration radii of small particles in the band of this particle type decrease due to more and more small particles concentrating in the periphery of this band. By the end of 280 s, the saturation of large and small particles [Fig. 13(a)] near the end wall gives rise to nearly constant gyration radii for the bands near the wall. For the region near the wall ( $0.78 < |z/Z| < 1$ ), the gyration radii of large and small particles increase from the end wall towards the central region. In the region of  $|z/Z| < 0.055$ , the nearly constant gyration radii for both particle types are mainly due to the extremely slow axial segregation in the central part.

#### IV. CONCLUSIONS

In this work, the numerical simulation of the flow of a binary-size mixture is conducted using DEM to understand the underlying mechanisms and axial distribution of the particle-scale dynamics associated with the axial segregation phenomenon in the 3-D rotating drum operating in the rolling regime. Macroscopically, the size difference between the particles leads to the fast radial segregation of small and large particles, respectively, to the radial core and radial periphery along the entire drum length before axial segregation becomes evident. The onset of axial segregation induced by the end walls is such that the large particles preferentially accumulate at the end walls, which causes the small particles to be propelled from the end walls and thereby leads to the formation of axial bands of small particles away from the end walls. Our numerical simulation provides new insights into the following aspects that are difficult to obtain experimentally.

Radial segregation does not affect the axial distribution of total mass and the mass fraction of each particle type along the drum length. However, axial segregation induces the redistribution of the total mass of particles along the drum length, such that axial bands of lower total mass appear at the end walls and adjacent axial bands of lower total mass appear slightly away from the end walls.

In such collision-dominated flow, the segregation results in greater non-dimensionalized collision force magnitudes for both the large and small particles associated with axial regions with fewer small particles. The space-time plot of non-dimensionalized collision forces indicates that axial bands also form, specifically in that axial bands of higher forces develop where the large particles dominate. Moreover,

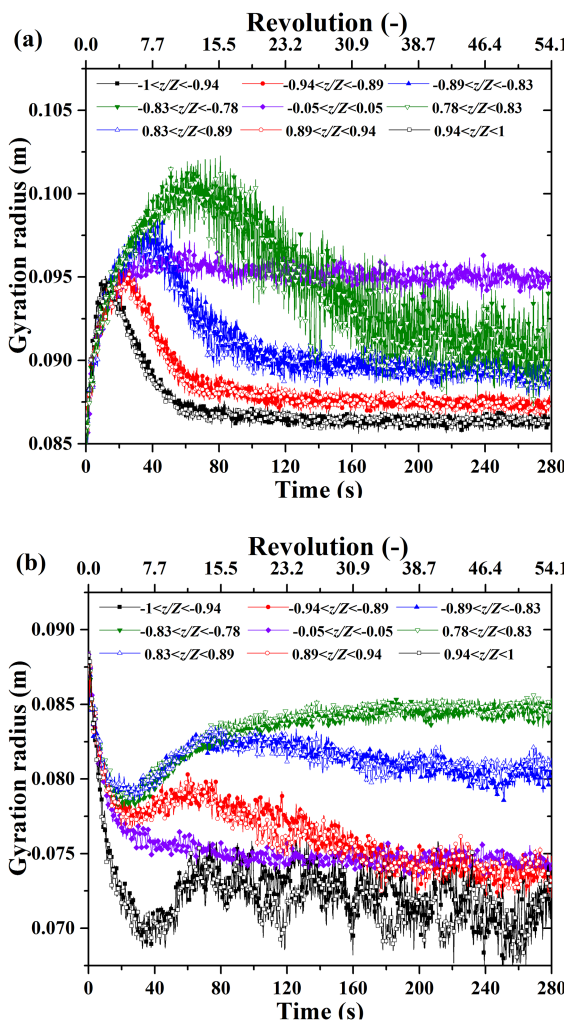


FIG. 13. Evolution of the gyration radius in the near wall region  $0.78 < |z/Z| < 1$  and the central region  $|z/Z| < 0.055$ : (a) large particles and (b) small particles.

the time-averaged non-dimensionalized collision forces with respect to drum length show similar trends along all the three directions.

The effect of the end walls on the axial flow direction is limited to a short axial distance from the end walls. While the scatter plots representing the flow directions towards and away from the end walls are different for each particle type at about 5% of the drum length away from the end wall, the scatter plots representing the two directions are similar for each particle type at approximately 25% of the drum length away from the end wall. Axial flow of both particle types in both the directions is observed at both axial positions, which indicate the dynamic axial exchanges.

Finally, the initial fast radial segregation increases and decreases the gyration radius of, respectively, the large and small particles. Then the axial segregation increases or decreases the gyration radius of the band of large and small particle types near the end walls, while that near the axial center changes only slightly.

## ACKNOWLEDGMENTS

The authors thank the financial support from the National Research Foundation (NRF), Prime Minister's Office, Singapore under its Campus for Research Excellence and Technological Enterprise (CREATE) program.

- <sup>1</sup>G. Seiden and P. J. Thomas, "Complexity, segregation, and pattern formation in rotating-drum flows," *Rev. Mod. Phys.* **83**, 1323 (2011).
- <sup>2</sup>S. D. Gupta, D. V. Khakhar, and S. K. Bhatia, "Axial segregation of particles in a horizontal rotating cylinder," *Chem. Eng. Sci.* **46**, 1513–1517 (1991).
- <sup>3</sup>D. V. Khakhar, J. J. McCarthy, and J. M. Ottino, "Radial segregation of granular mixtures in rotating cylinders," *Phys. Fluids* **9**, 3600–3614 (1997).
- <sup>4</sup>L. Prigozhin and H. Kalman, "Radial mixing and segregation of a binary mixture in a rotating drum: Model and experiment," *Phys. Rev. E* **57**, 2073 (1998).
- <sup>5</sup>K. M. Hill, D. V. Khakhar, J. F. Gilchrist, J. J. McCarthy, and J. M. Ottino, "Segregation-driven organization in chaotic granular flows," *Proc. Natl. Acad. Sci. U. S. A.* **96**, 11701–11706 (1999).
- <sup>6</sup>N. Jain, J. M. Ottino, and R. M. Lueptow, "Combined size and density segregation and mixing in noncircular tumblers," *Phys. Rev. E* **71**, 051301 (2005).
- <sup>7</sup>C. M. Dury and G. H. Ristow, "Competition of mixing and segregation in rotating cylinders," *Phys. Fluids* **11**, 1387–1394 (1999).
- <sup>8</sup>Y. Ding, R. Forster, J. P. K. Seville, and D. Parker, "Segregation of granular flow in the transverse plane of a rolling mode rotating drum," *Int. J. Multiphase Flow* **28**, 635–663 (2002).
- <sup>9</sup>N. Jain, J. M. Ottino, and R. M. Lueptow, "Regimes of segregation and mixing in combined size and density granular systems: An experimental study," *Granular Matter* **7**, 69–81 (2005).
- <sup>10</sup>K. M. Hill, G. Gioia, D. Amaravadi, and C. Winter, "Moon patterns, sun patterns, and wave breaking in rotating granular mixtures," *Complexity* **10**, 79–86 (2005).
- <sup>11</sup>I. Zuriguel, J. M. N. T. Gray, J. Peixinho, and T. Mullin, "Pattern selection by a granular wave in a rotating drum," *Phys. Rev. E* **73**, 061302 (2006).
- <sup>12</sup>I. Zuriguel, J. Peixinho, and T. Mullin, "Segregation pattern competition in a thin rotating drum," *Phys. Rev. E* **79**, 051303 (2009).
- <sup>13</sup>K. M. Hill and J. Zhang, "Kinematics of densely flowing granular mixtures," *Phys. Rev. E* **77**, 061303 (2008).
- <sup>14</sup>S. K. Hajra and D. V. Khakhar, "Radial segregation of ternary granular mixtures in rotating cylinders," *Granular Matter* **13**, 475–486 (2011).
- <sup>15</sup>R. D. P. East, P. McGuinness, F. Box, T. Mullin, and I. Zuriguel, "Granular segregation in a thin drum rotating with periodic modulation," *Phys. Rev. E* **90**, 052205 (2014).
- <sup>16</sup>Y. Oyama, "Axial segregation of granular materials," *Bull. Inst. Phys. Chem. Res.* **18**, 600 (1939).
- <sup>17</sup>P. Chen, J. M. Ottino, and R. M. Lueptow, "Onset mechanism for granular axial band formation in rotating tumblers," *Phys. Rev. Lett.* **104**, 188002 (2010).
- <sup>18</sup>K. Choo, T. C. A. Molteno, and S. W. Morris, "Travelling granular segregation patterns in a long drum mixer," *Phys. Rev. Lett.* **79**, 2975–2978 (1997).
- <sup>19</sup>Z. S. Khan, W. A. Tokaruk, and S. W. Morris, "Oscillatory granular segregation in a long drum mixer," *Europhys. Lett. (EPL)* **66**, 212 (2004).
- <sup>20</sup>H. P. Kuo, R. C. Hsu, and Y. C. Hsiao, "Investigation of axial segregation in a rotating drum," *Powder Technol.* **153**, 196–203 (2005).
- <sup>21</sup>G. Juarez, J. M. Ottino, and R. M. Lueptow, "Axial band scaling for bidisperse mixtures in granular tumblers," *Phys. Rev. E* **78**, 031306 (2008).
- <sup>22</sup>E. Alizadeh, O. Dubé, F. Bertrand, and J. Chaouki, "Characterization of mixing and size segregation in a rotating drum by a particle tracking method," *AIChE J.* **59**, 1894–1905 (2013).
- <sup>23</sup>D. Fischer, T. Finger, F. Angenstein, and R. Stannarius, "Diffusive and subdiffusive axial transport of granular material in rotating mixers," *Phys. Rev. E* **80**, 061302 (2009).
- <sup>24</sup>F. A. M. S. Tilo, M. Schröter, and R. Stannarius, "The mechanism of long-term coarsening of granular mixtures in rotating drums," *New J. Phys.* **17**, 093023 (2015).
- <sup>25</sup>C. Windows-Yule, B. J. Scheper, A. J. van der Horn, N. Hainsworth, J. Saunders, D. J. Parker, and A. R. Thornton, "Understanding and exploiting competing segregation mechanisms in horizontally rotated granular media," *New J. Phys.* **18**, 023013 (2016).
- <sup>26</sup>M. Mehrabadi and S. Subramanian, "Mechanism of kinetic energy transfer in homogeneous bidisperse gas-solid flow and its implications for segregation," *Phys. Fluids* **29**, 020714 (2017).
- <sup>27</sup>P. A. Cundall and O. D. L. Strack, "A discrete numerical model for granular assemblies," *Geotechnique* **29**, 47–65 (1979).
- <sup>28</sup>D. C. Rapaport, "Simulational studies of axial granular segregation in a rotating cylinder," *Phys. Rev. E* **65**, 061306 (2002).
- <sup>29</sup>D. C. Rapaport, "Simulated three-component granular segregation in a rotating drum," *Phys. Rev. E* **76**, 041302 (2007).
- <sup>30</sup>N. Taberlet, M. Newey, P. Richard, and W. Losert, "On axial segregation in a tumbler: An experimental and numerical study," *J. Stat. Mech.: Theory Exp.* **2006**, P07013.
- <sup>31</sup>E. Alizadeh, F. Bertrand, and J. Chaouki, "Comparison of DEM results and Lagrangian experimental data for the flow and mixing of granules in a rotating drum," *AIChE J.* **60**, 60–75 (2014).
- <sup>32</sup>J. M. N. T. Gray, "Granular flow in partially filled slowly rotating drums," *J. Fluid Mech.* **441**, 1–29 (2001).
- <sup>33</sup>M. Rasouli, O. Dubé, F. Bertrand, and J. Chaouki, "Investigating the dynamics of cylindrical particles in a rotating drum using multiple radioactive particle tracking," *AIChE J.* **8**, 2622–2634 (2016).
- <sup>34</sup>J. Mellmann, "The transverse motion of solids in rotating cylinders—forms of motion and transition behavior," *Powder Technol.* **118**, 251–270 (2001).
- <sup>35</sup>P. Umbanhowar, J. M. Ottino, and S. J. Fiedor, "Dynamics of axial segregation in granular slurries: Parallel experiments and influence of aspect ratio and periodic tilting," *Phys. Rev. E* **73**, 041303 (2006).
- <sup>36</sup>M. Nakagawa, "Axial segregation of granular flows in a horizontal rotating cylinder," *Chem. Eng. Sci.* **49**, 2540–2544 (1994).
- <sup>37</sup>J. A. P. C. Gabriel, "Transition to centrifuging granular flow in rotating tumblers: A modified Froude number," *New J. Phys.* **13**, 053055 (2011).
- <sup>38</sup>A. Voigt, J. Stadler, H. G. Niessen, L. Naji, R. Stannarius, and T. Finger, "Coarsening of axial segregation patterns of slurries in a horizontally rotating drum," *Phys. Rev. E* **74**, 031312 (2006).
- <sup>39</sup>A. Di Renzo and F. P. Di Maio, "Comparison of contact-force models for the simulation of collisions in DEM-based granular flow codes," *Chem. Eng. Sci.* **59**, 525–541 (2004).
- <sup>40</sup>S. Yang, A. Cahyadi, J. Wang, and J. W. Chew, "DEM study of granular flow characteristics in the active and passive regions of a three-dimensional rotating drum," *AIChE J.* **62**, 3874–3888 (2016).
- <sup>41</sup>K. W. Desmond and E. R. Weeks, "Influence of particle size distribution on random close packing of spheres," *Phys. Rev. E* **90**, 022204 (2014).
- <sup>42</sup>S. W. Meier, R. M. Lueptow, and J. M. Ottino, "A dynamical systems approach to mixing and segregation of granular materials in tumblers," *Adv. Phys.* **56**, 757–827 (2007).
- <sup>43</sup>J. M. N. T. Gray and K. Hutter, "Pattern formation in granular avalanches," *Continuum Mech. Thermodyn.* **9**, 341–345 (1997).

- <sup>44</sup>S. Yang, Y. Sun, L. Zhang, and J. W. Chew, "Segregation dynamics of a binary-size mixture in a three-dimensional rotating drum," *Chem. Eng. Sci.* **172**, 652–666 (2017).
- <sup>45</sup>P. Chen, J. M. Ottino, and R. M. Lueptow, "Granular axial band formation in rotating tumblers: A discrete element method study," *New J. Phys.* **13**, 055021 (2011).
- <sup>46</sup>I. S. Aranson and L. S. Tsimring, "Dynamics of axial separation in long rotating drums," *Phys. Rev. Lett.* **82**, 4643–4646 (1999).
- <sup>47</sup>C. R. J. Charles, Z. S. Khan, and S. W. Morris, "Pattern scaling in axial segregation," *Granular Matter* **8**, 1–3 (2006).
- <sup>48</sup>S. Inagaki, H. Ebata, and K. Yoshikawa, "Steadily oscillating axial bands of binary granules in a nearly filled coaxial cylinder," *Phys. Rev. E* **91**, 010201 (2015).
- <sup>49</sup>S. Inagaki and K. Yoshikawa, "Traveling wave of segregation in a highly filled rotating drum," *Phys. Rev. Lett.* **105**, 118001 (2010).